Journal of Materials Science & Technology 135 (2023) 156–169

Contents lists available at ScienceDirect

Journal of Materials Science & Technology

journal homepage: www.elsevier.com/locate/jmst

Research Article

In situ nanomechanical characterization of hydrogen effects on nickel-based alloy 725 under different metallurgical conditions

Xu Lu[a], Yan Ma[b], Ding Peng[c], Roy Johnsen[a], Dong Wang[a,*]

[a] Department of Mechanical and Industrial Engineering, Norwegian University of Science and Technology (NTNU), 7491 Trondheim, Norway
[b] Max-Planck-Institut für Eisenforschung GmbH, 40237 Düsseldorf, Germany
[c] Department of Physics, Norwegian University of Science and Technology (NTNU), 7491 Trondheim, Norway

ARTICLE INFO

Article history:
Received 4 March 2022
Revised 16 June 2022
Accepted 7 July 2022
Available online 3 August 2022

Keywords:
Hydrogen
Nickel-based alloy
In situ nanoindentation
Precipitates
Dislocation nucleation
Hardness

ABSTRACT

The effect of hydrogen on the surface morphology and nanomechanical properties of Ni-based Alloy 725 under solution-annealed (SA) and precipitation-hardened (API) conditions was thoroughly studied. The investigation involved in situ nanoindentation testing, microscopy characterization, statistical analysis, and numerical simulation approaches. The results showed the distinctive effects of hydrogen on the pop-in and hardness in the SA and API samples. For the SA sample, hydrogen mainly dissolved as solid solute in the matrix, causing enhanced lattice friction on the dislocation motion and increasing the internal stress *via* lattice expansion. Thus, an enhanced hardness, a reduced pop-in width/load ratio, and numerous surface steps were detected in the presence of hydrogen. For the API sample, the strengthening γ'' phases were the stress concentrators, and the dislocations nucleated heterogeneously, demonstrating indistinctive pop-in phenomena. Furthermore, the precipitates in the API sample affected the trapping behavior of hydrogen, thereby resulting in the hardness change, which reflected the competition between solution hardening in the matrix and vacancy softening mechanism in precipitates.

1. Introduction

Ni-based alloys are widely used in the oil and gas industry because of their outstanding mechanical properties and high resistance to both oxidation and corrosion in harsh environments [1]. Their high strength is mainly attributed to solid solution strengthening achieved by the addition of multiple alloying elements (e.g., Mo, Cr, and Nb) and precipitation hardening due to proper heat treatments [2–5]. Additionally, Mo and Cr are responsible for the excellent corrosion resistance; they form a stable oxide barrier layer and inhibit corrosion [1]. However, the presence of hydrogen deteriorates the positive effect, leading to unforeseen structural material failure. This severe degradation of mechanical properties caused by hydrogen is known as hydrogen embrittlement [6]. Although Ni-based alloys show better resistance to fracture and corrosion than most other face-centered cubic (FCC) alloys, it has been widely reported that hydrogen-induced cracking leads to a drastic reduction in ductility in Ni-based alloys, resulting in ductile-to-brittle fracture transition [7–10].

Hydrogen embrittlement has been extensively studied using several proposed mechanisms, among which the most invoked ones are hydrogen-enhanced localized plasticity [11,12], hydrogen-enhanced decohesion [13,14], hydrogen-enhanced strain-induced vacancy formation [15–17], and the Defactant mechanism [18,19]. Despite years of study, none of the aforementioned mechanisms can exclusively explain all hydrogen embrittlement phenomena. This is due to the complexity of hydrogen embrittlement, which depends on multiple factors, including microstructure, mechanical testing conditions, and hydrogen trapping and diffusion [20–22]. Thus, a single phenomenon often is explained on the basis of the synergistic effects of several mechanisms.

Regarding hydrogen embrittlement in Ni-based alloys, both hydrogen-assisted intergranular failure [23–25] and transgranular failure [8,26] have been documented in previous studies. For the intergranular fracture, different types of grain boundaries were studied by in situ bicrystalline micropillar compression tests on Alloy 725 [27]. The grain boundaries could suppress dislocation transmission in the presence of hydrogen owing to the hydrogen pinning effect, leading to dislocation pileups at grain boundaries, thereby contributing to elevated local stress, which could further induce intergranular cracking. Moreover, the coherent twin boundaries were identified as the sites most susceptible to hydrogen-

* Corresponding author.
E-mail address: dong.wang@ntnu.no (D. Wang).

https://doi.org/10.1016/j.jmst.2022.07.006

induced crack initiation, and the low Miller-index facets reportedly had excellent hydrogen embrittlement resistance in Alloy 725 [28,29]. For the transgranular fracture, the cracks in Alloy 718 were typically nucleated at the intersections of planar dislocation slip bands in the hydrogen-charged region because of the interaction between hydrogen and dislocations along the active slip planes with the highest Schmid factor [8,30]. Moreover, the precipitates in Ni-based alloys play an important role in void and crack formation because hydrogen segregates from the precipitates and promotes dislocation–hydrogen interplay at the interfaces [8,31]. Although tremendous efforts have been dedicated to studying the hydrogen-assisted degradation behavior using macroscale tensile tests, the nanomechanical response of Ni alloys in hydrogen environments has scarcely been explored. In particular, the interactions among hydrogen, dislocations, and strengthening phases cannot be fully revealed by conventional large-scale tensile tests. This literature gap hinders the understanding of the effect of hydrogen on local deformation behavior. Therefore, a small-scale testing approach is necessary to study the hydrogen–dislocation interactions in a confined region.

Nanoindentation has been recognized as an appropriate method for measuring the nanomechanical response in a small stress field. Mechanical properties, such as Young's modulus and hardness, as well as dislocation nucleation and multiplication can be detected in a confined volume by recording high-resolution load–displacement (L–D) data [32,33]. Moreover, in situ electrochemical nanoindentation (ECNI) was developed by integrating nanoindentation with in situ hydrogen charging [34–36]. Thus, the effect of hydrogen on the nanomechanical properties can be easily determined with a better understanding of the hydrogen embrittlement mechanisms. In this study, in situ ECNI tests were performed on Alloy 725 under different metallurgical conditions, *i.e.*, solution annealing (SA) and precipitation hardening (in accordance with the American Petroleum Institute standard, API), to thoroughly reveal the effect of hydrogen on the nanomechanical properties. Furthermore, the role of precipitates in hydrogen-affected dislocation nucleation and hardness change was demonstrated to better the understanding of the hydrogen-assisted degradation mechanism and pave the way for designing hydrogen-tolerant alloys.

2. Experimental

2.1. Materials and sample preparation

Laboratory-melt alloy 725 was investigated in this study. Its nominal composition is presented in Table 1. The alloy was melted using a vacuum induction furnace and forged to a bar with a length of 133 mm and a diameter of 12.5 mm. After forging, the alloy was heat-treated under two different conditions: SA and API. For the SA condition, the alloy was solution-annealed at 1038 °C for 2 h, followed by water quenching. For the API condition, the annealing process was followed by two aging steps. The alloy was aged first at 732 °C for 8 h and then at 621 °C for 8 h, followed by air cooling. The Alloy 725 samples after SA and API heat treatments would henceforth be referred to as SA and API, respectively. The bars were further sliced into discs with a thickness of 5 mm by electrical discharge machining for the in situ ECNI test. Afterwards, disc samples were prepared *via* a sequence of mechanical grinding using 200–000 grit SiC papers and polishing down to a 1 μm diamond suspension. Electropolishing was performed as the final step in a methanol/H_2SO_4 electrolyte at 26 V for 30 s to remove the deformation layer induced by the previous mechanical polishing processes.

Table 1
Nominal composition of Alloy 725 (in wt%) studied herein.

Ni	Fe	Cr	Nb	Mo	Ti	Al
Bal.	10.1	19.7	3.6	7.3	1.4	<0.1
Mn	**C**	**Si**	**S**	**P**	**N**	
<0.02	<0.01	<0.1	<0.001	<0.005	trace	

2.2. In situ ECNI test

The in situ ECNI test was performed using a Hysitron TriboIndenter TI 950 equipped with a long-shaft Berkovich diamond tip. The tip was specially designed for in situ applications and can be used for indentation and surface imaging through an electrolyte. A three-electrode electrochemical cell consisting of a platinum plate as the counter electrode, an Hg/Hg_2SO_4 reference electrode (all potentials in the article are measured with reference to this potential), and a test sample as the working electrode was designed for in situ hydrogen charging. Additional details about the in situ ECNI setup can be found in Ref. [34]. The electrolyte used for hydrogen charging was a 2:1 volume mixture of glycerol and H_3PO_4. This electrolyte has been proven as a good candidate for hydrogen charging in small-scale mechanical testing on nickel-based alloys, because it ensures a corrosion-free surface after long-term hydrogen charging [9,37,38]. Prior to the in situ ECNI test, electron backscatter diffraction analysis was performed on the specimens to identify the desired grains with a normal direction of <111> for the indentation testing, thereby eliminating the influence of different crystallographic orientations on the testing results.

Nanoindentation test was first performed in air without hydrogen charging as the reference condition. Then, hydrogen charging was sequentially applied at two different current densities of 0.1 and 1 mA/cm^2 (referred to as H1 and H2, respectively) to yield different hydrogen concentrations on the sample surface. The sample was precharged for 3 h under each condition prior to the nanoindentation test to ensure a constant hydrogen concentration in the subsurface region. After the cathodic hydrogen charging process, an anodic discharging step was applied at 100 mV (in the passive zone) for 10 h, followed by nanoindentation test to check the reversibility of the nanomechanical properties after hydrogen desorption. The indentation tests were performed during electrochemical charging/discharging in an in situ manner. The amount of charged hydrogen after each charging procedure was further determined by the thermal desorption technique, which will be introduced in detail in Section 2.4. During the in situ ECNI test, scanning probe microscopy (SPM) images were scanned after each charging/discharging process to track the changes in surface topography. For a given alloy, the same sample was subjected to different hydrogen conditions and tests. The sample after in situ ECNI test was taken out and rinsed carefully. The tested grain was further characterized to check the position of each indent. All the indents that were located outside the grain or on the inclusions were eliminated from data analysis.

The load function was operated in the load control mode; the loading rate was 8000 μN/s up to the peak load of 2000 μN, with a holding time of 0.45 s. Then, the unloading segment started at -8000 μN/s from the peak load and continued up to 10% of the peak load, with an additional 0.25 s holding for the drift correction, followed by further unloading to 0. For both alloys, at least 18 indentations were performed per testing condition to guarantee the reproducibility of the results.

2.3. Microstructural characterization

After the sample surface preparation, the microstructures of both the SA and API samples were characterized by high-resolution scanning electron microscopy (SEM, Quanta 650 FEG, Thermo Fisher Scientific Inc.). The precipitates were further characterized

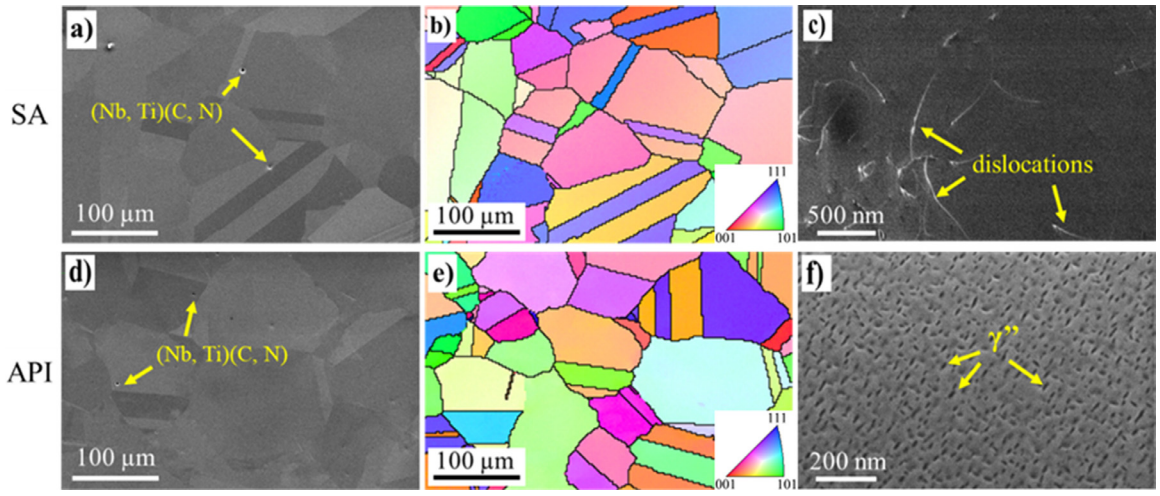

Fig. 1. SEM images (a, d) with the corresponding inverse pole figure maps (b, e), and the ECC images (c, f) of the solution-annealed (SA) (a–c) and precipitation-hardened (API) (d–f) samples showing the dislocation and precipitate distribution.

by transmission electron microscopy (TEM, JEOL JEM-ARM200F) on a lamella sample prepared using the focused ion beam (FIB). The elemental partitioning between the nanosized precipitates and matrix was characterized by atom probe tomography (APT). The FIB-prepared needle specimen was characterized using a local electrode atom probe 4000X HR instrument operated in laser-pulsing mode with laser energy of 10 pJ and a pulse frequency of 250 kHz. The temperature of the analysis chamber was maintained at −213.15 °C (60 K). The APT data were reconstructed using IVAS 3.8.0 (CAMECA Scientific Instruments, Madison, WI). In addition, electron channeling contrast imaging (ECCI) was performed before and after the in situ ECNI test to probe the microstructural changes induced by hydrogen charging. ECCI measurements were performed at an acceleration voltage of 30 kV and a working distance of ~5 mm. Moreover, the indented imprints under different conditions were examined and compared by ECCI after the in situ ECNI test.

2.4. Thermal desorption spectroscopy

Thermal desorption spectroscopy (TDS) was performed to determine the amount of dissolved hydrogen during the different cathodic charging procedures. The TDS test was applied to both the SA and API samples that underwent H1 and H2 hydrogen charging conditions. TDS measurements were performed using Bruker G4 PHOENIX DH combined with a mass spectrometry detector (ESD 100, InProcess Instruments, Germany). The samples were heated from 30 to 700 °C at a heating rate of 0.28 °C/s. The dwell time between hydrogen charging and start of the TDS measurement was controlled to <2 min to minimize hydrogen outgassing.

3. Results

3.1. Microstructural analysis

The microstructures of the SA and API samples are shown in Fig. 1. The SEM results combined with the normal direction-inverse pole figure maps show that both samples have a polycrystalline FCC structure with an equiaxed grain morphology and randomly distributed annealing twins. The average grain size is 84.8 μm for the SA sample and 97.4 μm for the API sample. This relatively large grain size enables all indentations to be performed within a single grain, thereby eliminating the effect of different crystallographic orientations. Block-shaped carbides and nitrides enriched with Nb and Ti ((Nb, Ti)(C, N)) are detected in both alloys (Fig. 1(a) and (d)), as determined by energy dispersive spectroscopy in our pre-

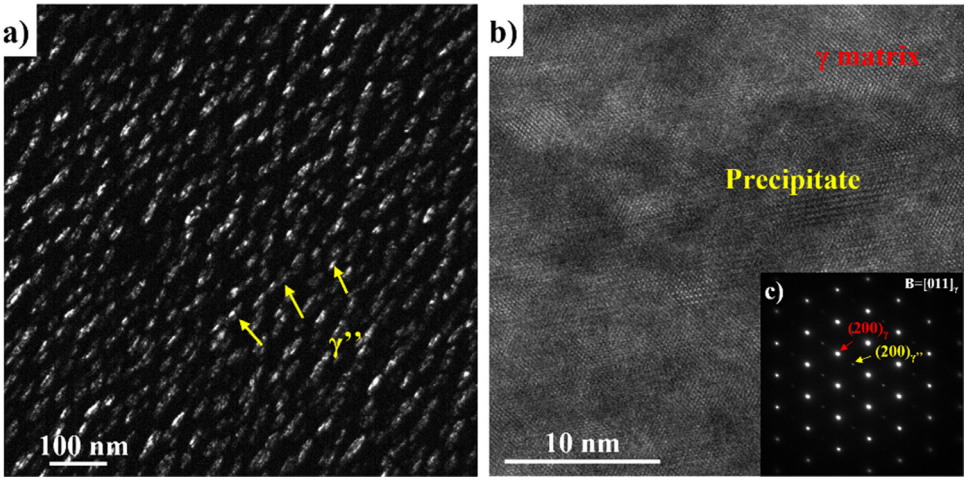

Fig. 2. (a) Dark field TEM micrograph showing the precipitate distribution and (b) HRTEM image of the API sample containing γ matrix and γ'' precipitate; (c) corresponding SAD pattern along zone axis $[011]_{\gamma}$ showing the orientation relationship between matrix and precipitate.

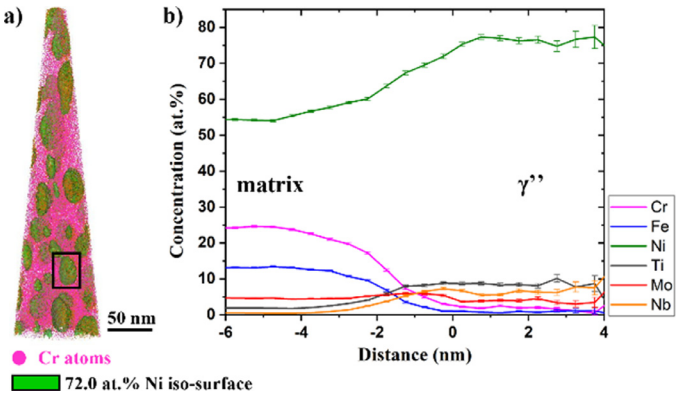

Fig. 3. Element distribution of precipitate studied by APT, showing (a) 3D atom map of Alloy 725 sample; (b) proximity histogram profile across the interface and matrix marked in (a).

vious study [9]. The major difference between the two samples is observed in the ECC images (Fig. 1(c) and (f)). For the SA sample, the matrix after the annealing process exhibits a "clean" structure containing a few randomly distributed dislocations. The dislocation density is estimated to be 3.1 × 10^{12} m^{-2} with an average dislocation spacing of 560 nm using the two-dimensional approach, *i.e.*, by counting the number of dislocations over the entire imaging area. In contrast, the API sample entirely consists of homogeneously distributed precipitates in the matrix. The precipitates, defined as γ'', have the chemical formula Ni_3Nb and a body-centered tetragonal $D0_{22}$ structure. Fig. 2(a) shows the dark field TEM image of disc-shaped γ'' in the matrix with an average length of 25 nm and a width of 5 nm. The precipitates were viewed side-on, where the long axis is parallel to the $(200)_{\gamma}$. The high-resolution TEM image and the corresponding selected diffraction pattern demonstrate that γ'' and the matrix share an orientation relationship of $(100)_{\gamma''}$ // $(100)_{\gamma}$. In addition, their interfaces exhibit high coherency. The chemical composition of the γ'' precipitate was further analyzed by APT. Fig. 3(a) shows the 3D atom map of the Alloy 725 sample. The concentration profile across the interface of the selected γ'' precipitate and matrix demonstrates enrichment in Ni (~74.5 at.%), Nb (~8.30 at.%), and Ti (~8.59 at.%) in the γ'' precipitates and depletion of Cr (~1.92 at.%) and Fe (~0.92 at.%) with reference to the matrix. Furthermore, the density of the γ" precipitates in the API sample is calculated as 8.2 × 10^2 μm^{-2} with an average distance of less than 10 nm [9].

3.2. Morphology change and imprints analysis

The SPM images depict the morphology information after each charging/discharging step, as shown in Fig. 4. Fig. 4(a) and (f) shows the original surface of the SA and API samples in air before testing, respectively. The surfaces of both samples are clean after electropolishing, with extremely low roughness values. The arithmetic average roughness R_a was determined as (2.73±0.88) nm and (3.76±1.34) nm for the SA and API samples, respectively. The relatively irregular topography of the API (Fig. 4(f)) is due to the fine γ" precipitates in the matrix, which cannot be evenly removed by electropolishing. After the indentation test in air, no morphological change in the surface is detected, except for the limited plastic area around the indents. Upon hydrogen charging, there are topographic differences between the two samples. For the SA sample, a few surface steps are observed after the low charging current density at H1 (Fig. 4(c)). These surface steps are multidirectional and become more noticeable when the charging current density is further increased to H2 (Fig. 4(d)). After the anodic discharging process, the steps remain on the surface, as shown in the SPM image (Fig. 4(e)). In contrast, the topography of the API sample remains unchanged during the entire testing (Fig. 4(h–j)). The roughness value R_a is determined as (3.69±1.18) nm, (3.80±1.41) nm, and (3.74±0.95) nm under H1, H2, and anodic condition, respectively. It indicates that the surface roughness remains roughly constant during the ECNI test when compared with the roughness in air condition as (3.76±1.34) nm. No surface step is detected, regardless of the charging and discharging conditions. It needs to mention here that the observed surface steps in the SA sample were due to hydrogen charging, and indentation did not contribute to this behavior. This was further proved by SPM analysis (shown in Fig. S1 of the supplementary document) on two other samples from both SA and API materials, where only hydrogen charging with the same parameter was carried out and the surface showed the same behavior as Fig. 4.

The phenomenon of surface steps was further characterized by ECCI, as shown in Fig. 5. The initial microstructure of the SA sample, which is shown in Fig. 1(c), contains randomly distributed dislocations without detectable surface steps. After the test, the surface steps are clearly detectable, as shown in Fig. 5(a–d). It is worth noting that the ECCI was performed after the entire in situ ECNI test. Therefore, the surface steps detected in air (Fig. 5(b)) pertain to those produced by the subsequent hydrogen-charging processes because for each alloy, the same sample was used throughout the test. Fig. 5(b–d) demonstrates the representative indents under the air, H1, and H2 conditions, respectively. The surface steps are accumulated by parallel dislocations, which are marked by yellow arrows, along the {111} slip traces. Moreover, the dimension of the surface plasticity can be estimated from the ECC images. The dislocations appear as white curved lines or dots on a dark background, indicating the interaction between linear dislocations and the sample surface. The surface plasticity zone consists of abundant dislocations, appearing shiny white around the indents marked by the yellow dashed circles. The size of plastic zone is determined as the radius of a circle that covers most of dislocations excluding the single dislocations reside far away from the indent center. This was supported by a finite-element simulation study from Durst et al., where the nanoindentation induced plastic zone is designated as the area with higher than 1–2% plastic strain [39]. Moreover, Zhang et al. performed ECCI analysis on nanoindents to determine the plastic zone [40]. They proposed that the highest dislocation density area determining the plastic zone is approximately half of the total dislocation area including the far resided single dislocations. Therefore, the radius of the surface plasticity zone of the SA sample in air (Fig. 5(b)) is measured to be (0.65±0.03) μm, while it reduces by 9.2% to (0.59±0.02) μm and 15.4% to (0.55±0.02) μm under H1 and H2 conditions, respectively (Fig. 5(c, d)). It needs to mention that the nanoindentation test was conducted with a load control mode, which might yield different indent sizes under different conditions due to the hydrogen affected hardness. For the SA sample, the radii of indents are (0.339±0.038) μm, (0.323±0.032) μm, and (0.313±0.038) μm under air, H1, and H2 condition, respectively. The change of indent size is 4.9% and 7.7% for H1 and H2 condition, respectively. Though a higher shrinkage of the plastic zone (9.2% for H1 and 15.4% for H2) induced by hydrogen was observed taken the reduced indent size into consideration, the displacement control mode is a better way to compare the plastic area for the future study.

For the API sample, no clear surface change is detected after hydrogen charging, which is consistent with the SPM results shown in Fig. 4(f–j). Detailed analysis on the topography change is shown in Fig. S2 of the supplementary document. It needs to mention here that the SPM and ECCI techniques are insufficient to distinguish the slip lines with few Burgers vectors in a precipitate-contained microstructure. The TEM analysis close to the indents is suggested to check the slip lines in detail. Moreover, the surface

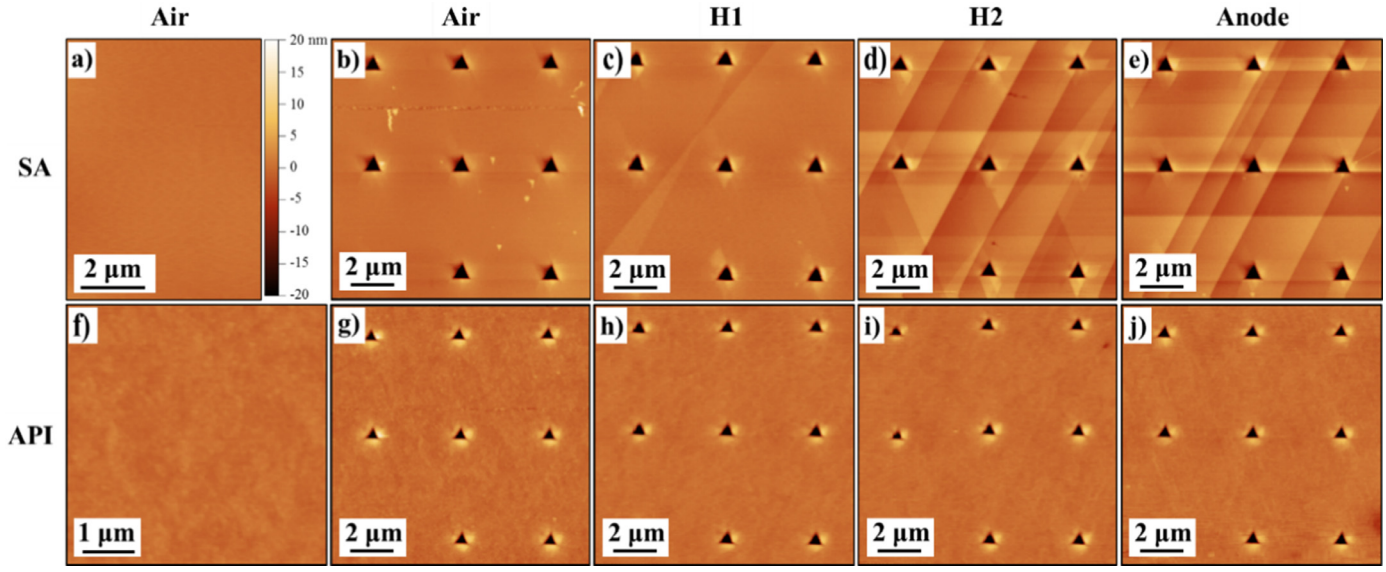

Fig. 4. SPM images during in situ ECNI test. (a–e) are the images of the SA sample, and (f–j) are the images of the API sample. The topography change during the ECNI test was presented.

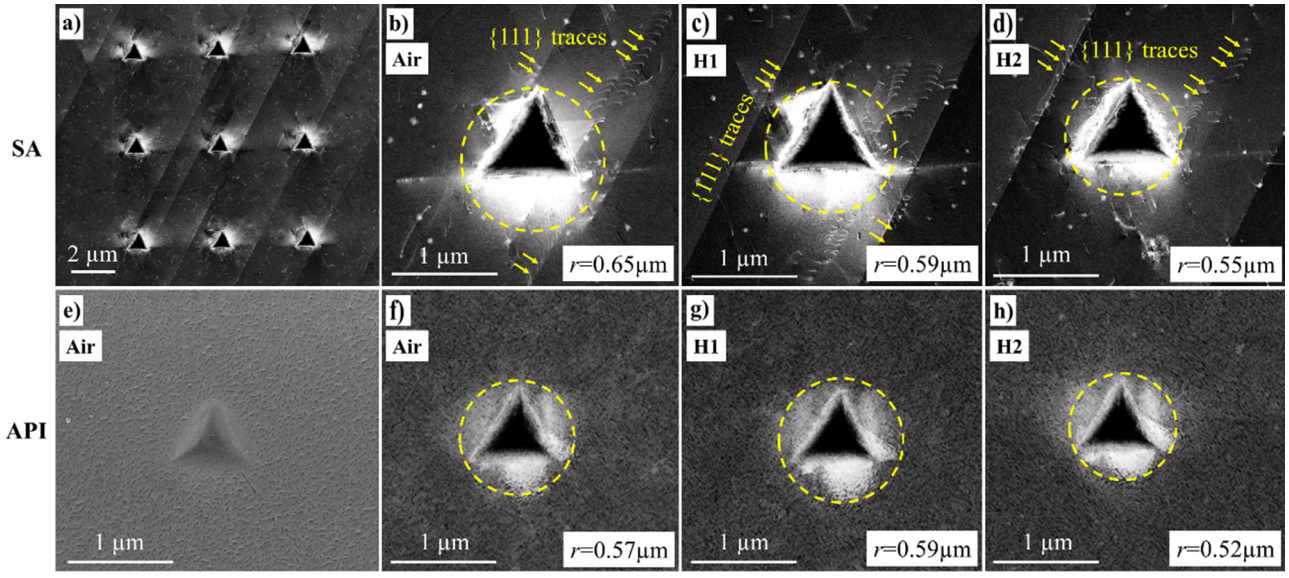

Fig. 5. (a–d) ECC image of the SA sample after in situ ECNI, showing the feature of surface steps and the plastic zones marked by yellow dashed circles. (e) SEM image of the indent of the API sample in air and the ECC images of the representative indents of the API sample under (f) air, (g) H1, and (h) H2 conditions with the marked plastic zones.

plasticity zone in air is measured to be (0.57±0.03) μm. Interestingly, it increases to (0.59±0.02) μm under H1 condition. When the severe charging condition H2 is applied, the surface plasticity zone reduces by 8.8% from that in air to (0.52±0.03) μm.

3.3. Nanomechanical properties

The L–D curves of the SA and API samples under different hydrogen charging/discharging conditions are presented in Fig. 6. At least 18 indentations were performed under each condition, and the results are highly reproducible. A typical L–D curve of the nanoindentation test consists of four stages: initial elastic loading, sudden displacement burst (pop-in), subsequent elastoplastic loading, and final elastic unloading. For the SA sample, the aforementioned stages are clearly identifiable in the L–D curves (Fig. 6(a–d)), while the pop-ins are chaotic and barely distinguishable in the L–D curves of the API sample (Fig. 6(e–h)). Another clear difference between the two samples is the residual depth. Specifically, the SA sample has a much larger residual depth than the API sample. Moreover, hydrogen-induced alterations can be observed in the L–D curves of both samples. Because each segment of the L–D curve reflects a specific nanomechanical property, the difference between the two samples, as well as the effect of hydrogen will be discussed in detail in the following sections.

3.3.1. Pop-in behavior

Pop-in is a unique behavior of load-controlled nanoindentation tests; it is characterized by a sudden displacement burst that appears as a plateau in the L–D curve. Pop-in has been proven to be an important parameter that shows the transition from elastic to plastic deformation [41]. It can also indicate the phase transformation or surface oxide layer breakage [42–45]. In the current study, the pop-in phenomenon is clearly observed in the L–D curves of the SA sample with a probability of ~100%, regardless of the

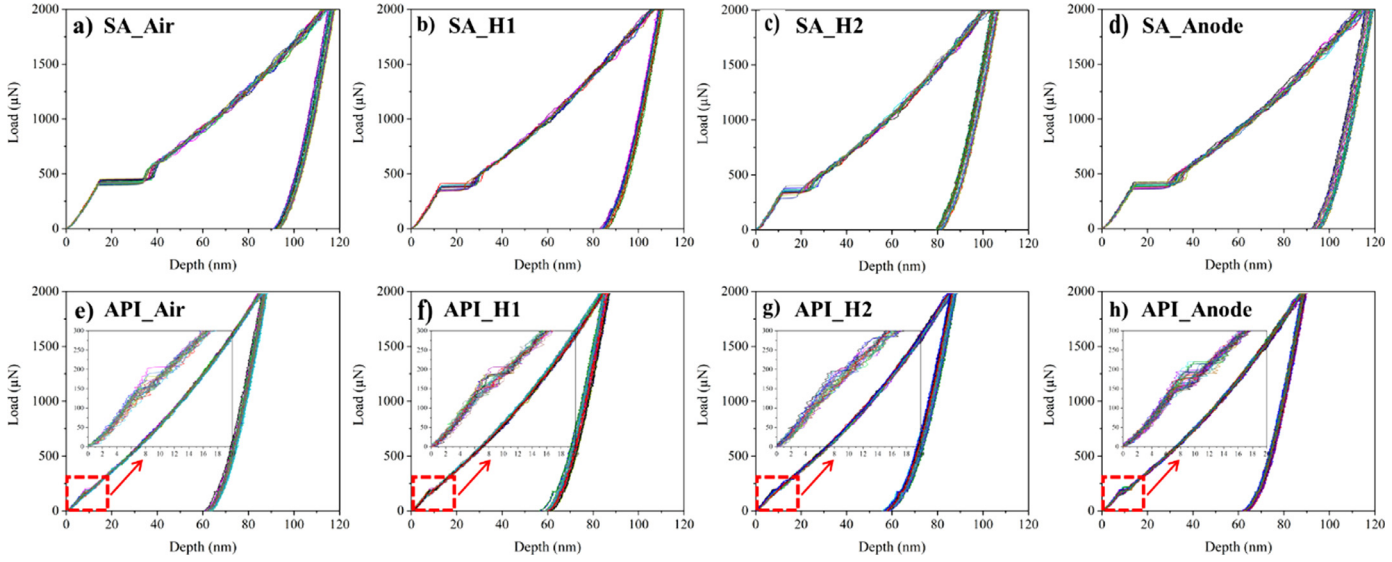

Fig. 6. Load–displacement curves under different hydrogen charging/discharging conditions, (a–d) are the curves of the SA sample, (e–h) are the curves of the API sample. The insets show the detailed information of hydrogen-reduced pop-in load.

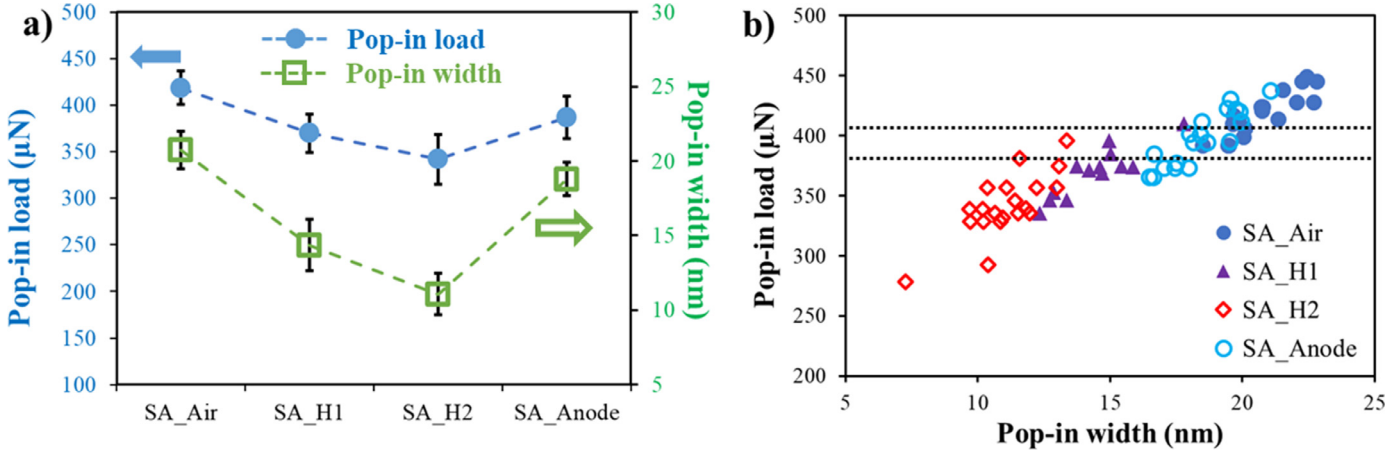

Fig. 7. Cumulative and reversible effect of hydrogen on pop-ins including (a) average pop-in load and width with standard deviations and (b) pop-in load and width from each load–displacement curve of the SA sample under different hydrogen conditions.

testing conditions. The mean values of the pop-in load and pop-in width of the SA sample under different testing conditions are shown in Fig. 7(a). In general, the pop-in behavior of the SA sample has good reproducibility under each testing condition. The introduction of hydrogen has a cumulative, reversible effect on both the pop-in load and width. Specifically, the pop-in load under H1 condition is 369.9 μN, which is 11.5% less than that in air (418.1 μN). When a higher concentration of hydrogen is applied under the H2 condition, the pop-in load is further reduced by 18.2% to 341.9 μN. After the total desorption of hydrogen under anodic conditions, the pop-in load recovers to 397.1 μN, differing with the load in air by only 4.4%. This difference might be caused by the trapped hydrogen in the microstructure that could not diffuse out during the anodic discharging process. Similarly, hydrogen reduces the pop-in width from 20.7 nm in air to 14.3 (30.6% reduction) and 11.1 nm (46.2% reduction) under H1 and H2 conditions, respectively. After anodic discharging, the pop-in width recovers to 18.7 nm. Although the dissolved hydrogen decreases both the pop-in load and width, the reduction effect is more pronounced on pop-in width than that on pop-in load. This trend can be better depicted by plotting the values of the pop-in load versus pop-in width for each L–D curve, as shown in Fig. 7(b). It can be seen that the load–width relationship is linear under each condition. However, the linear relations between different testing groups show different slopes and intercepts. In particular, a linear relationship under hydrogen charging conditions is observed with a cumulative, reversible leftward trend from the linear relationship in air. A highly pronounced reduction effect of hydrogen on the pop-in width is evinced. In contrast, the pop-in behavior of the API sample is difficult to distinguish under each testing condition. As shown in the subfigures in Fig. 6(e–h), the occurrence probability of a pop-in in the API sample is less than 22% with a pop-in width of less than 3 nm. Moreover, neither the pop-in load and width nor the occurrence probability exhibits a definite trend under the different testing conditions.

3.3.2. Hardness

The hardness data of the SA and API samples under different testing conditions are shown in Fig. 8. Fig. 8a shows the cumulative frequency distribution, and Fig. 8(b) shows the mean values with the corresponding standard deviations. The hardness value, H was calculated from the unloading portion of the L–D curve using the Oliver–Pharr method $H = \frac{P_{max}}{A_c}$ [46]. Here, the P_{max} is the maximum applied load during the nanoindentation test, A_c is the projected area function, which represents the contact area as a function of the contact depth h_c. Fig. 8(a) shows that the hardness value for each condition presents a high reproducibility with

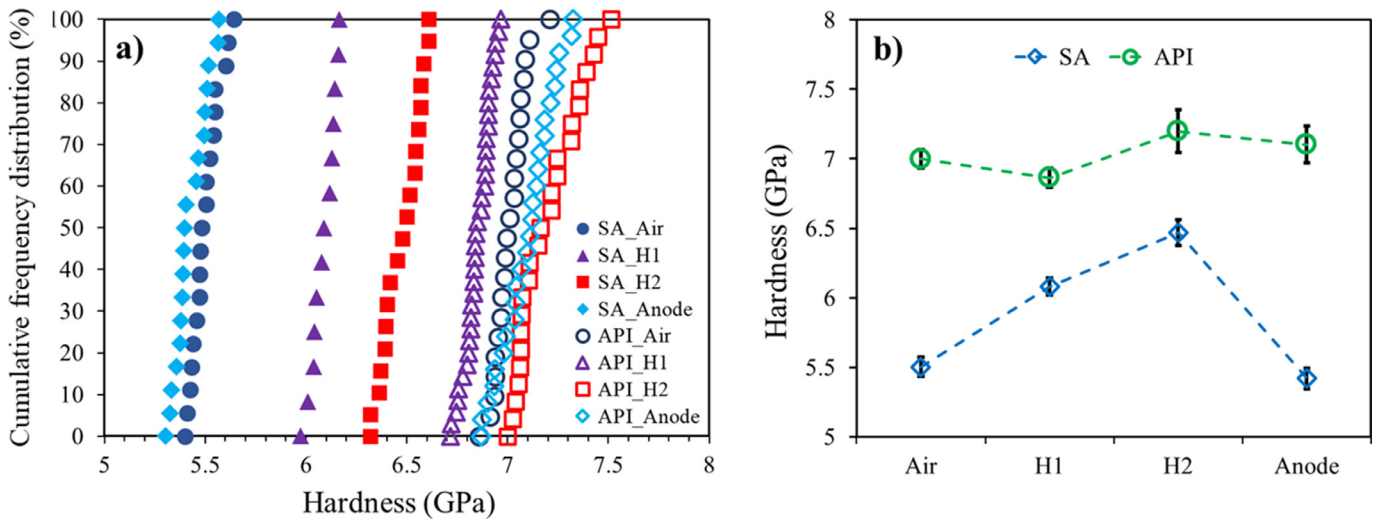

Fig. 8. Hydrogen effect on hardness value. (a) Cumulative frequency distribution and (b) average hardness values of the SA and API samples along with the standard deviations under different hydrogen conditions.

a small deviation, which is further proven by the small standard deviations shown in Fig. 8(b). In addition, the difference between the two samples is clearly observable; the API sample has a significantly higher hardness than the SA sample. Moreover, the intensity of the hydrogen effect on the hardness is also different. Specifically, at a lower hydrogen concentration (H1 condition), the hardness of the SA sample increases by 10.5% from 5.50 GPa in air to 6.08 GPa, while the hardness of the API sample surprisingly decreases by 2.0% from 7.00 GPa in air to 6.86 GPa. After charging at a higher hydrogen concentration (H2 condition), the hardness of the SA sample further increases by 17.5% to 6.47 GPa, and that of the API also increases, by 2.8% to 7.20 GPa. Overall, hydrogen has a more pronounced effect on the SA sample than on the API sample. After hydrogen desorption in the anodic condition, the hardness values in both SA and API samples recover to their original values in air with a difference of 1.5% and 1.4%, respectively.

4. Discussion

4.1. Hydrogen effect on the surface steps

The SPM images in Fig. 4 demonstrate the formation of surface steps in the SA sample after hydrogen charging. The surface steps thus formed become highly condensed and close-packed when exposed to a higher hydrogen concentration. These surface steps were further determined by ECCI (Fig. 5) as the accumulation of parallel dislocations along the {111} planes, which are the close-packed planes of the FCC structure. Thus, plastic deformation occurs on the surface of the SA sample during the hydrogen charging process, and the as-formed dislocations slip along the {111} planes, leaving surface steps on the sample surface. The preparation of the sample surface and installation of electrochemical charging cell were performed with special care, and no extra stress was expected. Therefore, the dissolved hydrogen is the only possible cause of plastic deformation.

It has been reported that hydrogen dissolved in interstitial sites can cause crystal lattice distortion of the host metal with an internal stress [47–49]. To determine the hydrogen-induced internal stress, the amount of dissolved hydrogen in the SA sample was first quantified by TDS, and the spectra are shown in Fig. 9(a). The amounts of hydrogen were defined as 0.287 and 0.830 wppm after charging under H1 and H2 conditions, respectively. Because Alloy 725 is an FCC-structured alloy with relatively low hydrogen diffusivity, the saturation level cannot be reached after 3 h of charging and hence, a hydrogen gradient, where the hydrogen concentration gradually decreases with the depth from the surface, is expected. The surface concentration can be determined by [50]:

$$C_s = \frac{hC_M}{4}\sqrt{\frac{\pi}{Dt}}, \tag{1}$$

where h is the sample thickness, C_M is the overall amount of dissolved hydrogen determined by TDS analysis, t is the hydrogen charging time, and D is the diffusion coefficient, which was determined as 1.23×10^{-15} m^2/s for the SA sample using $D = 4.06 \times 10^{-7}\exp(-\frac{48.63}{RT})$, as proposed for a similar Ni-based superalloy [51]. Then, the hydrogen distribution $C(x,t)$ as a function of the depth and charging time can be correspondingly obtained from the thick plate model as follows [52,53]:

$$\frac{C(x,t)-C_0}{C_s-C_0} = 1 - \mathrm{erf}\left(\frac{x}{\sqrt{4Dt}}\right), \tag{2}$$

$$\mathrm{erf}(u) = \frac{2}{\sqrt{\pi}}\int_0^u \exp\left(-u^2\right)\mathrm{d}u. \tag{3}$$

Here, C_0 is the bulk concentration before charging and was set to zero. The calculated hydrogen distribution is shown in Fig. 9(c). For the SA sample, the surface hydrogen content is determined as 164.2 and 496.7 wppm under H1 and H2 charging conditions, respectively.

On the basis of the highest hydrogen content on sample surface, the expansion of the lattice volume $\Delta V/V$ can be determined as a function of the atomic ratio between hydrogen and the host metal C_H, lattice volume charge with one dissolved hydrogen atom $\Delta\nu$, and mean volume of the metal atom Ω as [54]:

$$\Delta V/V = C_H(\Delta\nu/\Omega). \tag{4}$$

C_H can be calculated on the basis of the hydrogen content in wppm and molar mass of hydrogen and host metal. The molar mass of the studied alloy was theoretically determined to be 58.99 g/mol according to its chemical composition (Table 1). The value of $\Delta\nu/\Omega$ was adopted as 0.28, as reported for Ni [55]. Moreover, it has been proposed that the lattice parameter change $\Delta a/a$ is related to the volume expansion as $\frac{\Delta a}{a} = \frac{1}{3}\frac{\Delta V}{V}$ when the hydrogen atoms randomly occupy the interstitial sites and the crystal expands isotropically [47]. Therefore, the internal stress due to lat-

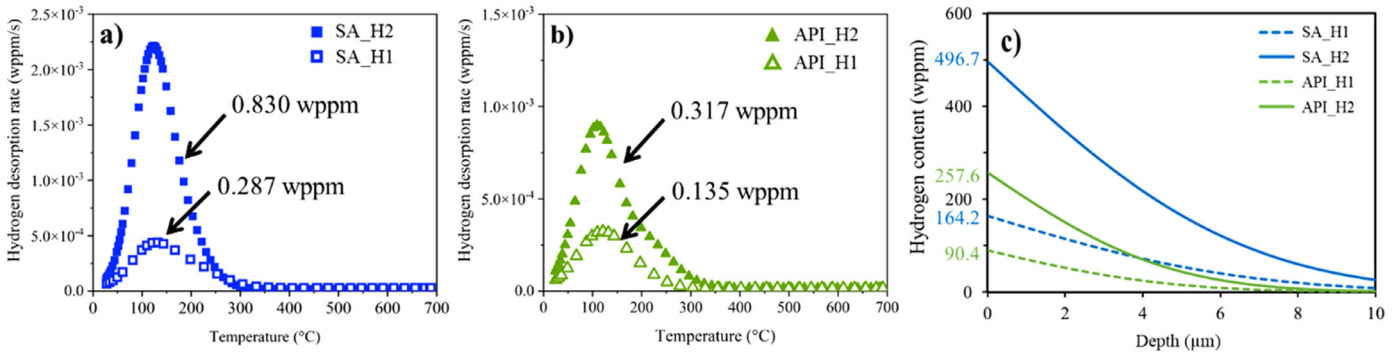

Fig. 9. Hydrogen content and distribution under different conditions. TDS spectra of SA (a) and API (b) samples after hydrogen charging under H1 and H2 conditions. (c) Distribution of hydrogen as a function of depth from the specimen surface.

tice expansion σ_i can be estimated as follows [56]:

$$\sigma_i = \frac{E}{2\nu} \cdot \frac{\Delta a}{a}, \tag{5}$$

where E is Young's modulus and ν is Poisson's ratio. On the basis of previous studies, the Young's modulus and Poisson's ratio were set to 204 GPa and 0.31, respectively [51,57]. Then, the maximum internal stress happened on the sample surface due to dissolved-hydrogen-induced lattice expansion was estimated to be 297.5 and 900.2 MPa for the SA sample under H1 and H2 charging conditions, respectively. It decreases by the depth due to the hydrogen concentration gradient. Moreover, the yield strength of the SA sample was measured as 269.8 MPa, which is smaller than the hydrogen-induced internal stress. As a result, the total stored elastic energy excesses the elastic limitation and triggers plastic deformation with dislocation nucleation and slip along the {111} planes to the sample surface, resulting in the surface steps in the SA sample.

In contrast, the API sample exhibits a non-changed surface quality throughout the ECNI test without any detectable surface variation. As determined by TDS, the API sample has a significantly lower hydrogen content than the SA sample (Fig. 9(b)). The corresponding hydrogen content distribution as a function of the depth is shown in Fig. 9(c). It is worth noting that the diffusion coefficient for the API sample is set to half of that of the SA sample because the γ'' precipitates in the API sample act as hydrogen trapping sites and considerably reduce the hydrogen diffusivity [58,59]. This has been proven by hydrogen permeation tests on similar Ni-based alloys [58,59]. Adopting the same approach, the internal stress in API alloy was calculated to be 163.7 and 466.8 MPa under H1 and H2 charging conditions, respectively. Owing to the precipitation hardening by γ'', the yield strength was measured as 733.3 MPa for the API alloy, which is higher than the calculated hydrogen-induced internal stress. In addition, based on the TDS spectra, a clear difference was observed between the SA and API samples. The SA sample manifest a relative symmetric peak, while the API sample shows a low temperature peak followed by a large shoulder, which is an indication of hydrogen trapping at the precipitates. The deconvolution of the TDS spectrum for API_H2 sample is shown in the supplementary document (Fig. S3 and Table S1). The area below the second peak is 1.5 times larger than the first peak, demonstrating that fine γ" precipitates can trap a large amount of hydrogen because of the high trapping energy (23–27 kJ/mol). Only part of the hydrogen was dissolved in interstitial sites, and this impacts the lattice expansion [31]. Therefore, the total stored elastic energy in the form of internal stress due to dissolved-hydrogen-induced lattice expansion was even lower than the estimated values. Consequently, plastic deformation is unfeasible in the API sample under the applied charging conditions and hence, surface steps are not observed.

4.2. Hydrogen effect on the pop-in behavior

Regarding the pop-in behavior of the SA and API samples, two main findings are obtained: (1) In the SA sample, a highly reproducible pop-in occurs with a probability of ~100% and is greatly impacted by the hydrogen concentration. In particular, both the pop-in load and width cumulatively decrease with an increase in hydrogen concentration (from H1 to H2 condition). Moreover, this decrease is reversible after the anodic degassing process. The highly recovered pop-in load behavior after anodic degassing indicates a pure hydrogen effect on the pop-in load during charging conditions. (2) In the API sample, most of the L–D curves do not exhibit pop-in, regardless of the testing conditions. Furthermore, no clear impact of hydrogen on the pop-in behavior is observed (Fig. 6(e–h)). These observations are discussed in the following sections.

4.2.1. Pop-in behavior of the SA sample

Pop-in has been proposed to result from dislocation nucleation [60], breakage of the surface oxide layer, or indents on the surface impurities [61]. The samples in this study were carefully prepared before testing and hence, the oxide layer and surface impurities were not expected. Therefore, the pop-in phenomena in the SA sample indicate either homogeneous dislocation nucleation due to the formation of a new dislocation in the defect-free region under the theoretical strength or heterogeneous dislocation nucleation caused by the activation of pre-existing defects that require a little stress. Comparing the maximum shear stress at the onset of pop-in with the theoretical strength is an efficient, straightforward method to determine the dislocation nucleation mechanism. According to continuum mechanics, the maximum shear stress τ_{max} with the corresponding depth $Z_{\tau_{max}}$ during a pop-in is calculated as follows [33]:

$$\tau_{max} = 0.31\left(\frac{6E_r^2}{\pi^3 R^2}P\right)^{\frac{1}{3}}, \tag{6}$$

$$Z_{\tau_{max}} = 0.48a_c = 0.48\left(\frac{3PR}{4E_r}\right)^{\frac{1}{3}}. \tag{7}$$

Here, P is the pop-in load, a_c is the contact area at the onset of pop-in, E_r is the reduced modulus, which can be determined from the Hertzian fitting of the elastic loading portion using $P(h) = \frac{4}{3}E_r h^{3/2}R^{1/2}$ [62]. R is the tip radius (0.98 μm) that was calibrated on the fused quartz. On the basis of Eq. 6, τ_{max} was calculated as 4.42, 4.33 and 4.24, and 4.40 GPa under air, H1 and H2 charging, and anodic discharging conditions, respectively. Using the same Young's modulus (204 GPa) and Poisson's ratio (0.31) as those in Section 4.1, the shear modulus μ was estimated to be 77.8 GPa. As a result, the τ_{max} of the SA sample was between μ/18.3 and

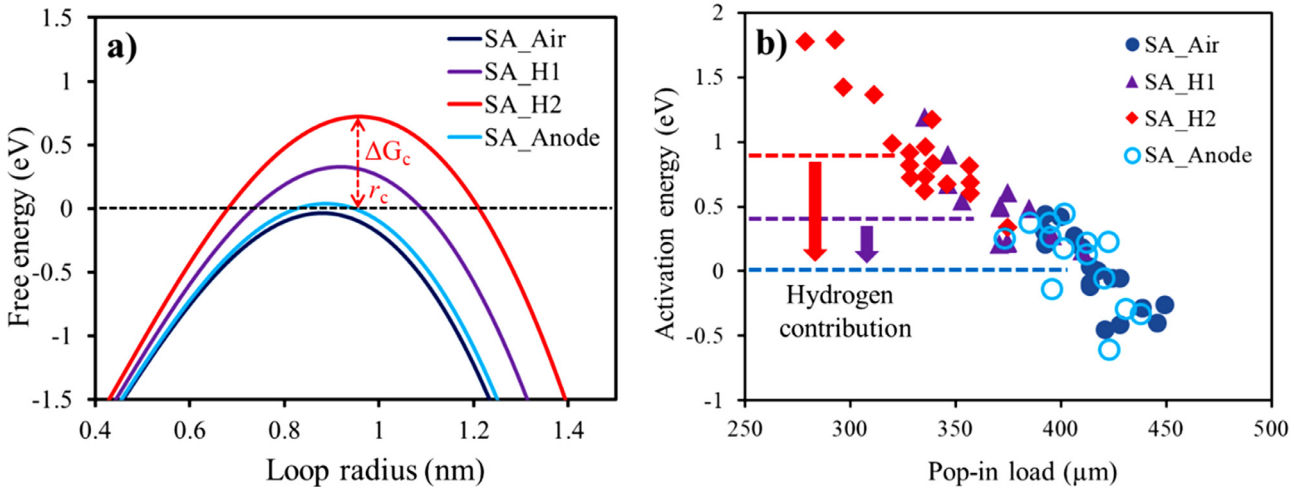

Fig. 10. (a) Gibbs free energy for homogeneous dislocation nucleation in the SA sample as a function of radius of the dislocation loop under different testing conditions. (b) Activation energy for dislocation nucleation at the onset of each pop-in, indicating a hydrogen reduced activation energy for dislocation nucleation.

μ/17.6, falling exactly in the range μ/5–μ/30, which corresponds to the theoretical shear strength of the material [63,64]. Therefore, the pop-in in the SA sample arises from the homogeneous dislocation nucleation. Moreover, after annealing, the SA sample has a very low dislocation density with an average spacing of 560 nm, as shown by ECCI (Fig. 1(c)). During nanoindentation, the pop-in occurs at an indentation depth of ~16 nm with approximately 52 nm of $Z_{\tau_{max}}$, where the maximum shear stress occurs. Therefore, the stress region is highly unlikely to contain pre-existing defects when the pop-in occurs; hence, the observed pop-in is attributed to homogeneous dislocation nucleation. Furthermore, a reduction in the pop-in load due to the presence of hydrogen has been also observed in other alloys such as TWIP steel, FeSi, and carbon steel [35,65,66] owing to hydrogen-enhanced homogeneous dislocation nucleation.

The enhancement in homogeneous dislocation nucleation by hydrogen in the SA sample can be directly and simply explained by the corresponding decrease in τ_{max} at the onset of pop-in, because τ_{max} cumulatively decreased upon introducing hydrogen, indicating easy nucleation of the dislocation. Moreover, the classical dislocation theory has been widely adopted to predict the free energy required for homogeneous dislocation nucleation [65]. Here, a similar approach was employed to calculate the Gibbs free energy ΔG for stable dislocation loop formation in the presence of applied shear stress, as follows:

$$\Delta G = 2\pi r W_{dis} - \pi r^2 b \tau_{max}, \quad (8)$$

$$W_{dis} = \frac{2-\upsilon}{1-\upsilon}\frac{\mu b^2}{8\pi}\left(\ln\frac{4r}{r_0} - 2\right), \quad (9)$$

where r is the dislocation loop radius, W_{dis} is the unit dislocation line energy, b is the Burgers vector, υ is Poisson's ratio, and r_0 is the dislocation core radius. The two terms on the right-hand side of Eq. (8), in order, depict the formation energy of a dislocation loop and external work done to expand the loop. Fig. 10(a) shows plots of free energy as a function of the dislocation loop radius for the SA samples under different testing conditions. The curves were obtained using the mean values of τ_{max} at the beginning of the pop-in load and other material constants that are shown in Table 2. Fig. 10(a) shows that the maximum free energy, defined as the activation energy, at the critical radius needs to be overcome to nucleate a thermodynamically stable dislocation loop, else the initial embryonic dislocation with a size less than r_c shrinks and vanishes [67,68]. This signifies that for a nanoindentation test under the applied shear stress, pop-in phenomena can only be observed when the activation energy is lower than the available thermal energy, which is a few tenths of eV at room temperature [69]. Fig. 10(b) shows the activation energy of each indentation test as a function of the corresponding pop-in load. Under hydrogen-free conditions (air and anode), the activation energy is nearly zero, and homogeneous dislocation nucleation is energetically favorable. As a result, pop-in is supposed to occur at the applied shear stress, which is consistent with the results shown in Fig. 6(a) and (d).

Table 2
Physical constants used to calculate free energy plots of homogeneous dislocation nucleation in the SA sample.

E (GPa)	μ (GPa)	υ	b (nm)	r_0 (nm)	R (μm)	τ_{max} (GPa)			
						Air	H1	H2	Anode
204	77.8	0.31	0.25	0.17	0.98	4.42	4.33	4.24	4.40

In contrast, the activation energy under hydrogen-charged conditions (H1 and H2) is higher than the available thermal energy at room temperature, indicating that the dislocation nucleation behavior is energetically unfavorable and no pop-in should occur at the applied shear stress. This is inconsistent with ~100% probability of pop-in behavior under hydrogen-charged conditions observed in Fig. 6(b) and (c). Therefore, the activation energy must be overcome. Hydrogen is the only difference between the tests under different conditions and the effect of hydrogen was not considered in the aforementioned energy calculation. Thus, hydrogen can promote homogeneous dislocation nucleation by decreasing the required activation energy. This is within the scope of "Defactant" concept proposed by Kirchheim [18,19,70], where the formation energy of defects (such as dislocations) is reduced in the presence of defactant solutes (such as hydrogen atoms) based on thermodynamic calculations.

Moreover, the pop-in load exhibits a linear relationship with the pop-in width under the same testing conditions, as shown in Fig. 7(b). However, this linear relationship is not constant between different testing conditions, where the impact of hydrogen on the pop-in width is more pronounced than that on the pop-in load. The detailed relationship between the pop-in load and width has been reported on the basis of the energy balance criterion, which proposes that the overall stored elastic energy before the pop-in is consumed by the plastic work during the pop-in process [71,72]. Since for a nanoindentation test on sample surface with relatively

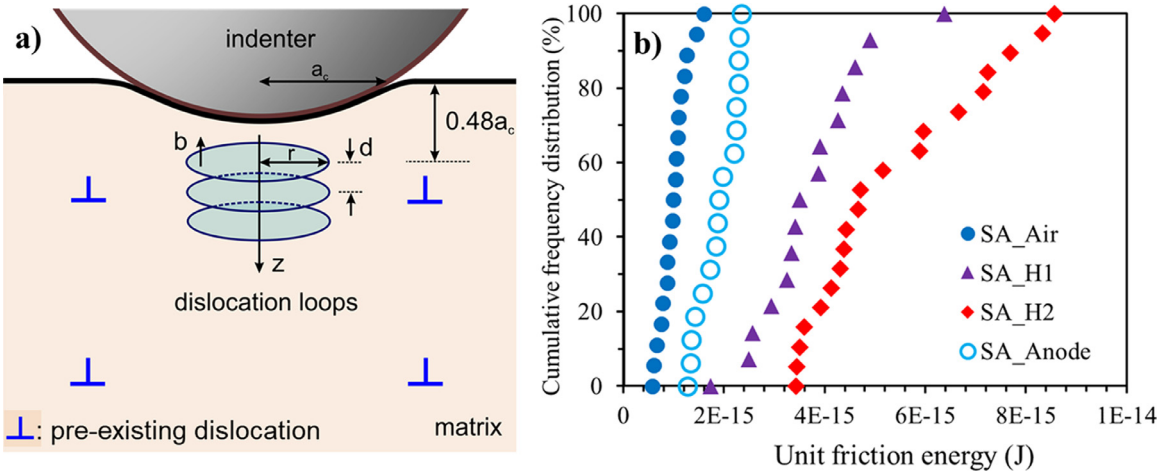

Fig. 11. (a) Schematic of prismatic dislocation loops generated during the pop-in process beneath the indenter. (b) Cumulative frequency distribution of unit friction energy for dislocation motion in the SA sample under different testing conditions.

low pre-existing dislocation density, the first dislocation is nucleated at the maximum shear stress beneath the indenter (with a depth of 0.48 a_c) at the beginning of the pop-in, followed by continuous dislocation multiplication and emission, which assumably forms a stack of prismatic dislocation loops at the end of the pop-in, as shown in Fig. 11(a). The total plastic work during pop-in includes the dislocation interaction energy, dislocation line energy, and friction energy on dislocation motion. A detailed study analyzing the interaction between hydrogen and dislocations focusing on the pop-in width *via* the aforementioned energy balance model is presented in Ref. [73]. By using the same energy model approach, the unit friction energy, defined as the energy required to move a dislocation by a distance of one burgers vector, can be calculated. Here the unit friction for each indentation test under different conditions is presented as the cumulative frequency distribution in Fig. 11(b), which shows that the mean unit friction energy for dislocation motion under hydrogen-free condition (in air) is 9.95 × 10^{-16} J and increases by 3.7 times (3.70 × 10^{-15}) and 5.4 times (5.36 × 10^{-15} J) under H1 and H2 conditions, respectively. After the hydrogen degassing under the anodic conditions, the unit friction energy recovers to 1.89 × 10^{-15} J, differing with the value in air by only 1.9 times. This minor difference may be caused by the trapped hydrogen, which cannot diffuse out during the anodic discharging process. Therefore, the highly pronounced reduction effect of hydrogen on the pop-in width can be attributed to hydrogen-enhanced lattice friction, which consumes more stored elastic energy and results in a fewer nucleated dislocations and a smaller pop-in width, compared to the behavior in the hydrogen-free condition, according to the solute drag theory [74].

4.2.2. Pop-in behavior of the API sample

In comparison to the ~100% pop-in occurrence probability observed in the SA sample, only ~20% of the L–D curves of the API sample show a pop-in phenomenon, regardless of the testing conditions. In addition, the pop-in load and width are much lower and smaller, respectively, with more deviations than those of the SA sample. The differences are due to the highly complex microstructure of the API sample. As shown in Fig. 1(f), the API sample contains evenly distributed fine γ" precipitates. The precipitates have an average size of 25 nm and a spacing of ~10 nm with a relatively high density of 8.2 × 10^2 μm^{-2}. During the nanoindentation test, these precipitates can act as lattice defects that affect the nanomechanical properties, especially the pop-in behavior. It has been reported when sufficient defects exist in the subsurface region, plastic deformation is carried out by heterogeneous dislocation nucleation rather than homogeneous dislocation nucleation [75,76]. Consequently, a pre-existing dislocation or defect, which requires much lower stress than the newly nucleated ones, is activated. As a result, plastic deformation occurs at a lower load, and the elastic–plastic transition is smoother, which may not be accompanied by a pop-in. Another possibility is that the fine γ" precipitates distributed in the subsurface act as stress concentrators during the indentation process, and the loading force is therefore overestimated, resulting in a much lower pop-in load.

Regarding the small pop-in width in the API sample, shown in Fig. 6(e–h), there are two possible explanations. First, a low pop-in load generally results in a small pop-in width, as shown in the linear load–width relationship in Fig. 7(b). Second, γ" precipitates in the API matrix obstruct the dislocation motion and increase the lattice friction, which can greatly reduce the pop-in width, as discussed in Section 4.4.2. As a result, a significantly small pop-in width (<3 nm) is observed in the API sample, with only ~20% occurrence probability. Moreover, Fig. 6(e–h) shows that hydrogen has no distinct effect on the pop-in load and width in the API sample, *i.e.*, the impact of hydrogen on the pop-in behavior of the API sample is not as pronounced as that of the SA sample and can be neglected compared to the impact of precipitates. The impact of defects on pop-in behavior has been reported in other studies as well. Wang et al. studied the influence of surface preparation on the pop-in behavior of single-crystal Mo with various surface mechanical damages and defects [77]. They observed that both the pop-in load and pop-in occurrence decreased with an increase in the pre-existing dislocation density *via* mechanical polishing. Jin et al. reported the impact of irradiation damage on pop-in behavior by introducing vacancies of different compositions *via* ion irradiation [78]. They found out that with an increase in the vacancies, the nucleation of the dislocations switched from homogeneous to heterogeneous with a clear pop-in load reduction. This study complements the understanding of the impact of defects on the pop-in behavior by reporting on the effect of the precipitate (another defect type) aside from dislocation and vacancy.

4.3. Hydrogen effect on hardness

The effect of hydrogen on the hardness is shown in Fig. 8. First, an obvious difference is observed between the SA and API samples. A recoverable, cumulative hydrogen-enhanced hardness behavior is observed in the SA sample. In contrast, the API sample exhibits softening under a relatively low hydrogen content (H1 condition),

Table 3
Strengthening constants of solute atoms in Ni (MPa At. Fraction $^{-1/2}$) [84].

Parameter	a_{Fe}	a_{Cr}	a_{Nb}	a_{Mo}	a_{Ti}	a_{Al}
Value	153	337	1183	1015	775	225

while a slight hardening occurs under a higher hydrogen content (H2 condition). The hardness also recovered to the value in the air condition, indicating a pure hydrogen effect during the charging process.

4.3.1. Hydrogen effect on hardness of the SA sample

In the nanoindentation test, the elastoplastic regime of the L–D curve describes the continuous hardening process, which will be studied in detail to reveal the hydrogen effect on hardness. On the basis of the Tabor relation [79], the elastoplastic loading P can be expressed as:

$$P = CA_c\sigma. \tag{10}$$

Here, $C = 3$ is the Tabor constant that transforms the plastic zone from a complex stress state into a uniaxial stress state [62]. A_c is the projected area that depends on the indentation depth and indenter shape. σ is the overall stress, including dislocation strengthening stress σ_{disl}, solid solution strengthening stress σ_{ss}, precipitation strengthening stress, and grain boundary strengthening stress.

For the SA sample, only σ_{disl} and σ_{ss} were considered under the hydrogen-free condition because the indentation tests were performed for a single grain and the SA sample contained no precipitates. σ_{disl} can be derived using the Taylor relation as [80]:

$$\sigma_{disl} = M\alpha\mu b\sqrt{\rho_{SSD} + \rho_{GND}}\ , \tag{11}$$

where $M = 3$ is the Taylor factor and α is an empirical factor that was set to 0.5 [81]. μ is the shear modulus, and b is the Burgers vector. ρ_{SSD} and ρ_{GND} are the densities of the statistically stored dislocations (SSD) and geometrically necessary dislocations (GND), respectively. The original ρ_{SSD} in the SA sample can be estimated as 3.1×10^{12} m^{-2} from the ECC image in Fig. 1(c). The ρ_{SSD} increases to 6.5×10^{12} m^{-2} after charging, as shown in Fig. 5, because of the hydrogen-induced surface slip lines. ρ_{GND} can be calculated according to the Nix–Gao model as follows [82]:

$$\rho_{GND} = \frac{3}{2}\frac{1}{f^3}\frac{\tan^2\theta}{bh}, \tag{12}$$

where f is the ratio between the radius of the plastic zone a_{pz} and contact area a_c. $\theta = 24.65°$ is the angle between the sample surface and the Berkovich indenter.

σ_{ss} was calculated on the basis of Gypen and Deruyttere's model [83], which expresses the total solid solution strengthening stress of a multicomponent alloy as follows:

$$\sigma_{ss} = \left[\sum\nolimits_i \left(a_i \cdot c_i^{1/2}\right)^2\right]^{1/2}. \tag{13}$$

Here, a_i and c_i are the strengthening constant and atomic concentration of solute i, respectively. Table 3, cited in Ref. [84], shows the strengthening constants of the main solute atoms in Ni. On the basis of the composition shown in Table 1, the value of σ_{ss} for the currently studied material was calculated as 327.1 MPa.

Under hydrogen charging conditions, the hydrogen atoms dissolve in the matrix as an interstitial element in the solid solution, which contributes to the solid solution strengthening by further impeding the dislocation motion. The additional solid solution strengthening stress provided by hydrogen is denoted as σ_H. Therefore, considering all the strengthening mechanisms, the Tabor-relation-based Nix–Gao model for the SA sample can be rewritten on the basis of Eqs. (10)–(13) as:

$$P = CM\alpha\mu bA_c\sqrt{\rho_{SSD} + \frac{3}{2}\frac{1}{f^3}\frac{\tan^2\theta}{bh}} + C(\sigma_{ss} + \sigma_H)A_c. \tag{14}$$

Under the hydrogen-free condition, the hydrogen contribution σ_H can be neglected. By fitting the elastoplastic regime of the L–D curves with the Tabor relation-based Nix–Gao model, a proportionality factor $f = 1.81$ is determined to yield a good fit, as shown in Fig. 12(a). Under the hydrogen-charging conditions, σ_H was integrated into the model. The same numerical fitting yields the results of $f = 1.77$ and $\sigma_H = 78$ MPa under H1 condition and $f = 1.75$ with $\sigma_H = 190$ MPa under H2 condition. In this study, the f value was determined by numerical fitting. Alternatively, the f value can also be calculated as the ratio between the radius of the plastic zone a_{pz} and contact area a_c, which is the original physical definition of f. a_{pz} can be estimated from Lawn's theory, which relies on the ratio between the Young's modulus and hardness *i.e.*, $(\frac{E}{H})$, and the residual indentation depth h_f as $a_{pz} = \varphi(\frac{E}{H})^{\frac{1}{3}}\tan^{\frac{1}{3}}(\theta)h_f$ [85]. $\varphi = 3.64$ is the geometric constant for the Berkovich indenter [86]. a_c can be measured as the size of the imprints from the ECC images (Fig. 5) or SPM images (Fig. 4). Using this approach, the f values were calculated as 1.82, 1.75, and 1.72 under air, H1, and H2 conditions, respectively, and are very close to the fitted f values. A hydrogen-reduced f factor is observed, which is consistent with the imprint topography analysis shown in Fig. 12(b–e). Because the f factor is the ratio between the radius of the plastic zone and the contact area, a reduced f factor indicates shrinkage in the plastic zone. Correspondingly, the 2D color-filled contour image of the imprint under the hydrogen-charged condition (Fig. 12(e)) shows a more pronounced shrinkage in plastic zone compared with that under the hydrogen-free condition (Fig. 12(d)). The shrinkage in plastic zone under the hydrogen charging condition is also proven by the ECC images in Fig. 5(b) and (d), indicating a hampered dislocation motion caused by the dissolved hydrogen. Therefore, on the basis of hydrogen-enhanced σ_H and hydrogen-reduced f factor, it can be proposed that the hardening effect of hydrogen on the SA sample is related to the hydrogen-impeded dislocation motion due to the increased lattice friction caused by the interstitially dissolved hydrogen. This finding is corroborated by the atomistic simulations conducted by Song and Curtin [74], who studied the effect of hydrogen on dislocation mobility at the nanoscale and proposed that hydrogen can generate a Cottrell-like atmosphere and hinder dislocation motion. On the other hand, Maxelon *et al.* used small angle neutron scattering technique to study the hydrogen distribution in the dilatation field dislocations, and they proposed that hydrogen forms narrow cylinders with random orientation along dislocations instead of forming Cottrell cloud and hence hinders the dislocation motion [87].

4.3.2. Hydrogen effect on hardness of the API sample

For the API sample, the hardness was significantly higher than that of the SA alloy before hydrogen charging in air. This relatively high hardness of the API alloy is attributed to precipitation strengthening. During plastic deformation, dislocations cut through γ'' *via* a shearing mechanism, resulting in enhanced strength and hardness. In contrast to the cumulatively increased hardness under hydrogen-charged conditions in the SA sample, the API sample softened under H1 charging potential and hardened under H2 charging potential.

This dual effect of hydrogen on hardness in the API sample was caused by the difference in hydrogen concentration and precipitate-affected hydrogen distribution. Specifically, under H1 charging potential, only 0.135 wppm of hydrogen dissolved in the material, as revealed by the TDS results in Fig. 9. In this case, the majority of hydrogen was trapped by the γ'' precipitates ow-

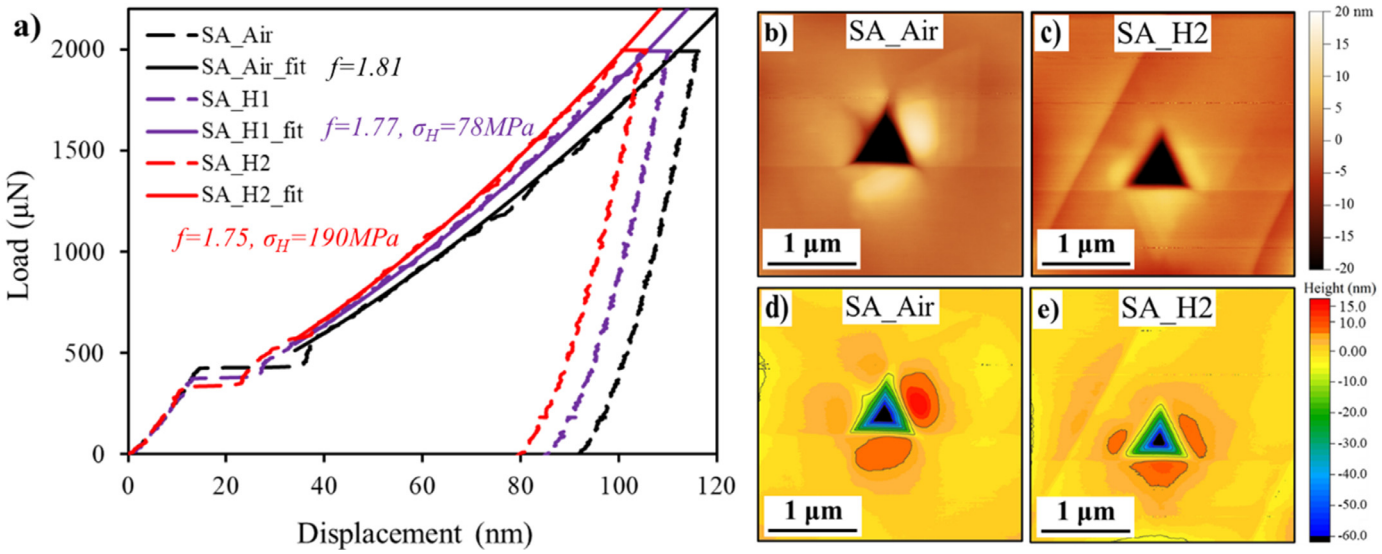

Fig. 12. (a) Representative L–D curves of the SA sample under different testing conditions; the elastoplastic part is fitted by the Tabor-relation-based Nix–Gao model showing the hydrogen induced friction on dislocation motion. (b, c) are the SPM images and (d, e) are the corresponding 2D color-filled contour plots of representative indents under the hydrogen-free and hydrogen-charged conditions, respectively, indicating a hydrogen reduced plastic area.

ing to their higher trapping energy than FCC matrix [31]. Zhang et al. observed the same hydrogen distribution by performing TDS and NanoSIMS techniques on Ni-based superalloys [31]. This uneven hydrogen distribution between the precipitates and matrix can have two consequences: (I) More hydrogen is adsorbed on the precipitates than on the matrix; this can result in high internal stress at the interface between the precipitates and matrix. In addition, highly intense interactions between hydrogen and dislocations can occur at the interface during plastic deformation. As a result, nanoscale voids may form and coalesce as vacancies along the interfaces, thereby reducing the hardness. The hydrogen-induced softening through the formation of voids and vacancies has been reported earlier *via* atomic simulations and experiments on Ni alloys [88–90]. (II) The amount of hydrogen, which is uniformly distributed in the matrix, is insufficient to impede dislocation motion. It has been proven that a little hydrogen can enhance the dislocation mobility by either reducing the Peierls stress [91] or nucleating the kink pairs [92], resulting in a hydrogen-induced softening effect. Therefore, due to a relatively small amount of hydrogen in the API alloy studied herein, the hydrogen that majorly trapped in the precipitates and minorly dissolved in the matrix work together resulting in an overall softening effect, as evidenced by the hardness reduction under H1 charging potential (Fig. 8(b)).

When additional hydrogen was introduced to the material under H2 charging condition, the amount of hydrogen in the precipitates reached the saturation value, because the γ'' precipitates have a higher hydrogen trapping energy but a much lower hydrogen solubility than the matrix [31]. Thus, a sufficiently large amount of hydrogen remained in the matrix. In this case, hydrogen is enough to form narrow cylinders around the dislocation lines, leading to resistance to dislocation motion and hydrogen-induced hardening. The hydrogen trapped in the precipitates in this condition still contributed to a softening effect, and the overall hydrogen effect on the hardness was a competition between solution hardening in the matrix and vacancy softening in precipitates. Here, the latter played a dominant role. This result suggests that the effect of hydrogen on the hardness of the API sample is determined by the hydrogen concentration in both the precipitates and matrix. Thus, it is possible to retard the hydrogen diffusion process in the matrix and delay the hydrogen-assisted mechanical degradation by pinning hydrogen at local traps, which can be manipulated by the type, size, and number density of the precipitates.

5. Conclusions

In this work, the effect of hydrogen on the surface integrity and nanomechanical properties of solution-annealed and precipitation-hardened Ni-based Alloy 725 samples was investigated using in situ nanoindentation together with numerical simulation approaches. The variations in the surface morphology, pop-in behavior, and hardness with hydrogen charging at different current densities and discharging were statistically analyzed and compared for the two samples. The main conclusions are summarized as follows:

(1) Surface steps were detected in the SA sample after hydrogen charging, and a much severe charging condition resulted in many condensed steps. From the TDS spectra, ECC images, and numerical calculations, the surface steps were determined as the accumulation of parallel dislocations due to plastic deformation, which was triggered by the hydrogen-induced internal stress due to the lattice expansion. However, the API alloy exhibited a non-changed surface without any surface step under the present hydrogen-charging conditions because the relatively little hydrogen in the matrix resulted in lower internal stress (163.7 MPa under H1 and 466.8 MPa under H2), compared to the yield stress (733.3 MPa).

(2) Pop-in phenomenon was observed in the SA sample with ~100% probability and high reproducibility, regardless of the testing conditions. Moreover, the pop-in load cumulatively decreased with the amount of dissolved hydrogen. The pop-ins in the SA sample indicated homogeneous dislocation nucleation, which was enhanced by hydrogen *via* reduction in the required activation energy according to the classical dislocation theory. However, only approximately 20% of the L–D curves of the API alloy exhibited pop-in phenomena, wherein the pop-in load was low with high deviations, because of the precipitate-induced heterogeneous dislocation nucleation and stress concentration, which resulted in a smooth elastic–plastic transition.

(3) Although both the pop-in load and width decreased owing to the hydrogen in the SA sample, the reduction effect was more

pronounced on the pop-in width. The energy balance model and statistical analysis showed that hydrogen could enhance lattice friction, which resulted in relatively few nucleated dislocations and a short pop-in width.

(4) For the SA sample, the hardness continuously increased with the amount of hydrogen. Using the Tabor-relation-based Nix–Gao model, the enhanced hardness was explained to have resulted from the hydrogen-enhanced lattice friction on the dislocation motion. However, a dual effect of hydrogen on hardness was observed in the API sample, *i.e.*, the sample softened under H1 but hardened under H2. This indicated the hydrogen-content-dependent hardness behavior of the API alloy, whose hardness was synergistically determined by solution hardening in the matrix and vacancy softening in precipitates.

Data availability

The data that support the findings of this study are available on request from the corresponding author. The data are not publicly available as the data also forms part of an ongoing study.

Acknowledgments

The authors acknowledge voestalpine BOHLER Edelstahl GmbH & Co KG for providing laboratory-scale Alloy 725 samples. The authors acknowledge the support provided by Research Council of Norway through the HyLINE (294739) and M-HEAT (294689) projects. D.P. acknowledges SFI Manufacturing, funded by the Research Council of Norway (237900) and the financial support from the Research Council of Norway to the NORTEM project (197405). The authors are greteful for the Steel Institute of the RWTH Aachen Univeristy for providing the atom probe facility.

Supplementary materials

Supplementary material associated with this article can be found, in the online version, at doi:10.1016/j.jmst.2022.07.006.

References

[1] L. Liu, J. Zhang, C. Ai, in: Encyclopedia of Materials: Metals and Allloys, Elsevier, Oxford, 2022, pp. 294–304.
[2] A.S. Ebner, S. Jakob, H. Clemens, R. Pippan, V. Maier-Kiener, S. He, W. Ecker, D. Scheiber, V.I. Razumovskiy, Acta Mater. 221 (2021) 117354.
[3] M.S. Hazarabedian, M.Z. Quadir, M. Iannuzzi, Mater. Charact. 171 (2021) 110770.
[4] D.M. Collins, N. D'Souza, C. Panwisawas, C. Papadaki, G.D. West, A. Kostka, P. Kontis, Acta Mater. 200 (2020) 959–970.
[5] P. Kontis, Z. Li, D.M. Collins, J. Cormier, D. Raabe, B. Gault, Scr. Mater. 145 (2018) 76–80.
[6] W.H. Johnson, in: Proceedings of the Royal Society London, 23, 1874, pp. 168–179.
[7] Z. Tarzimoghadam, D. Ponge, J. Klöwer, D. Raabe, Acta Mater. 128 (2017) 365–374.
[8] Z. Zhang, G. Obasi, R. Morana, M. Preuss, Acta Mater. 113 (2016) 272–283.
[9] X. Lu, Y. Ma, D. Wang, Mater. Sci. Eng. A 792 (2020) 139785.
[10] M.S. Hazarabedian, M. Iannuzzi, NPJ Mater. Degrad. 5 (2021) 39.
[11] H.K. Birnbaum, P. Sofronis, Mater. Sci. Eng. A 176 (1994) 191–202.
[12] P. Sofronis, I. Robertson, Phil. Mag. A 82 (2002) 3405–3413.
[13] R.A. Oriani, P.H. Josephic, Acta Metall. 22 (1974) 1065–1074.
[14] C.J. McMahon, Eng. Fract. Mech. 68 (2001) 773–788.
[15] M. Nagumo, Hydrogen related failure of steels - a new aspect, Mater. Sci. Technol. -Lond. 20 (2004) 940–950.
[16] A. Metsue, A. Oudriss, X. Feaugas, J. Alloy. Compd. 656 (2016) 555–567.
[17] A. Metsue, A. Oudriss, X. Feaugas, Comp. Mater. Sci. 151 (2018) 144–152.
[18] R. Kirchheim, Acta Mater. 55 (2007) 5129–5138.
[19] R. Kirchheim, Acta Mater. 55 (2007) 5139–5148.
[20] M.B. Djukic, G.M. Bakic, V. Sijacki Zeravcic, A. Sedmak, B. Rajicic, Eng. Fract. Mech. 216 (2019) 106528.
[21] B. Sun, D. Wang, X. Lu, D. Wan, D. Ponge, X. Zhang, Acta Metall. Sin.-Eng. Lett. 34 (2021) 741–754.
[22] B. Sun, W. Lu, B. Gault, R. Ding, S.K. Makineni, D. Wan, C.-H. Wu, H. Chen, D. Ponge, D. Raabe, Nat. Mater. 20 (2021) 1629–1634.
[23] S. Jothi, S.V. Merzlikin, T.N. Croft, J. Andersson, S.G.R. Brown, J. Alloy. Compd. 664 (2016) 664–681.
[24] A. Kimura, H.K. Birnbaum, Acta Metall. 36 (1988) 757–766.
[25] Y. Yao, X. Pang, K. Gao, Int. J. Hydrog. Energy 36 (2011) 5729–5738.
[26] P. Hicks, C. Altstetter, Metall. Transact. A 21 (1990) 365–372.
[27] X. Lu, D. Wang, J. Mater. Sci. Technol. 67 (2021) 243–253.
[28] J.P. Hanson, A. Bagri, J. Lind, P. Kenesei, R.M. Suter, S. Gradečak, M.J. Demkowicz, Nat. Commun. 9 (2018) 1–11.
[29] M. Seita, J.P. Hanson, S. Gradečak, M.J. Demkowicz, Nat. Commun. 6 (1) (2015) 6164.
[30] Z. Zhang, G. Obasi, R. Morana, M. Preuss, Scr. Mater. 140 (2017) 40–44.
[31] Z. Zhang, K.L. Moore, G. McMahon, R. Morana, M. Preuss, Corros. Sci. 146 (2019) 58–69.
[32] D.F. Bahr, D.E. Kramer, W.W. Gerberich, Acta Mater. 46 (1998) 3605–3617.
[33] C. Begau, A. Hartmaier, E.P. George, G.M. Pharr, Acta Mater. 59 (2011) 934–942.
[34] A. Barnoush, H. Vehoff, Scr. Mater. 55 (2006) 195–198.
[35] D. Wang, X. Lu, Y. Deng, X. Guo, A. Barnoush, Acta Mater. 166 (2019) 618–629.
[36] A.S. Ebner, E. Plesiutschnig, H. Clemens, R. Pippan, V. Maier-Kiener, Int. J. Hydrog. Energy 46 (2021) 38132–38143.
[37] X. Lu, D. Wang, D. Wan, Z.B. Zhang, N. Kheradmand, A. Barnoush, Acta Mater. 179 (2019) 36–48.
[38] G. Stenerud, R. Johnsen, J.S. Olsen, J.Y. He, A. Barnoush, Int. J. Hydrog. Energy 42 (2017) 15933–15942.
[39] K. Durst, B. Backes, M. Goken, Scr. Mater. 52 (2005) 1093–1097.
[40] J.L. Zhang, S. Zaefferer, D. Raabe, Mater. Sci. Eng. A-Struct. 636 (2015) 231–242.
[41] C. Zhu, Z.P. Lu, T.G. Nieh, Acta Mater. 61 (2013) 2993–3001.
[42] Y. Sato, S. Shinzato, T. Ohmura, T. Hatano, S. Ogata, Nat. Commun. 11 (2020) 4177.
[43] X. Lu, Y. Ma, M. Zamanzade, Y. Deng, D. Wang, W. Bleck, W.W. Song, A. Barnoush, Int. J. Hydrog. Energy 44 (2019) 20545–20551.
[44] S. Jiapeng, L. Cheng, J. Han, A. Ma, L. Fang, Sci. Rep. 7 (2017) 10282.
[45] D. Chrobak, K. Nordlund, R. Nowak, Phys. Rev. Lett. 98 (2007) 045502.
[46] W.C. Oliver, G.M. Pharr, J. Mater. Res. 19 (2004) 3–20.
[47] R. Kirchheim, A. Pundt, in: Hydrogen in Metals, Elsevier, 2014, pp. 2597–2705.
[48] D. Wang, X. Lu, Y. Deng, D. Wan, Z. Li, A. Barnoush, Intermetallics 114 (2019) 106605.
[49] D. Wang, X. Lu, D. Wan, Z. Li, A. Barnoush, Scr. Mater. 173 (2019) 56–60.
[50] A.E. Pontini, J.D. Hermida, Scr. Mater. 37 (1997) 1831–1837.
[51] J. Xu, X.K. Sun, Q.Q. Liu, W.X. Chen, Metall. Mater. Transact. A 25 (1994) 539–544.
[52] V. Olden, C. Thaulow, R. Johnsen, Mater. Des. 29 (2008) 1934–1948.
[53] X. Lu, D. Wang, R. Johnsen, Electrochim. Acta 421 (2022) 140477.
[54] M. Hoelzel, S.A. Danilkin, H. Ehrenberg, D.M. Toebbens, T.J. Udovic, H. Fuess, H. Wipf, Mater. Sci. Eng. A 384 (2004) 255–261.
[55] H.J. Bauer, G. Berninger, G. Zimmermann, Z. Naturforschung A 23 (1968) 2023–2029.
[56] A.S. Hassanien, A.A. Akl, Phys. B-Condens. Matter 473 (2015) 11–19.
[57] M. Fukuhara, A. Sanpei, J. Mater. Sci. Lett. 12 (1993) 1122–1124.
[58] J.J.M. Jebaraj, D.J. Morrison, I.I. Suni, Corros. Sci. 80 (2014) 517–522.
[59] A. Turnbull, R.G. Ballinger, I.S. Hwang, M.M. Morra, M. Psaila-Dombrowski, R.M. Gates, Metall. Trans. A 23 (1992) 3231–3244.
[60] X. Xiao, L. Yu, Int. J. Plast. 141 (2021) 102980.
[61] S.K. Venkataraman, D.L. Kohlstedt, W.W. Gerberich, J. Mater. Res. 8 (1993) 685–688.
[62] K.L. Johnson, Contact Mechanics, Cambridge University Press, Cambridge, 1987.
[63] Y. Xia, Y. Gao, G.M. Pharr, H. Bei, J. Mater. Res. 31 (2016) 2065–2075.
[64] J. Frenkel, Zur Theorie der Elastizitätsgrenze und der Festigkeit kristallinischer Körper 37(7) (1926) 572–609.
[65] A. Barnoush, H. Vehoff, Acta Mater. 58 (2010) 5274–5285.
[66] D. Wang, A.B. Hagen, D. Wan, X. Lu, R. Johnsen, Mater. Sci. Eng. A 824 (2021) 141819.
[67] S. Izumi, S. Yip, J. Appl. Phys. 104 (2008) 033513.
[68] S. Lee, A. Vaid, J. Im, B. Kim, A. Prakash, J. Guenole, D. Kiener, E. Bitzek, S.H. Oh, Nat. Commun. 11 (2020) 2367.
[69] A. Barnoush, M. Asgari, R. Johnsen, Scr. Mater. 66 (2012) 414–417.
[70] R. Kirchheim, Scr. Mater. 62 (2010) 67–70.
[71] A. Gouldstone, H.J. Koh, K.Y. Zeng, A.E. Giannakopoulos, S. Suresh, Acta Mater. 48 (2000) 2277–2295.
[72] Y. Shibutani, T. Tsuru, A. Koyama, Acta Mater. 55 (2007) 1813–1822.
[73] D. Wang, X. Lu, M. Lin, D. Wan, Z. Li, J. He, J. Roy, J. Mater. Sci. Technol. 98 (2021) 118–122.
[74] J. Song, W.A. Curtin, Acta Mater. 68 (2014) 61–69.
[75] K. Gan, D. Yan, S. Zhu, Z. Li, Acta Mater. 206 (2021) 116633.
[76] Y. Zhao, J.-M. Park, J.-i. Jang, U. Ramamurty, Acta Mater. 202 (2021) 124–134.
[77] Z.G. Wang, H. Bei, E.P. George, G.M. Pharr, Scr. Mater. 65 (2011) 469–472.
[78] K. Jin, Y. Xia, M. Crespillo, H. Xue, Y. Zhang, Y.F. Gao, H. Bei, Scr. Mater. 157 (2018) 49–53.
[79] D. Tabor, The Hardness of Metals, Oxford University Press, 2000.
[80] G.I. Taylor, Plastic Strain Met. 62 (1938) 307–324.
[81] K. Durst, B. Backes, O. Franke, M. Goken, Acta Mater. 54 (2006) 2547–2555.
[82] W.D. Nix, H.J. Gao, J. Mech. Phys. Solids 46 (1998) 411–425.
[83] L. Gypen, A. Deruyttere, J. Mater. Sci. 12 (1977) 1028–1033.
[84] H.A. Roth, C.L. Davis, R.C. Thomson, Metall. Mater.Transact. A 28 (1997) 1329–1335.
[85] B.R. Lawn, A.G. Evans, D.B. Marshall, J. Am Ceram. Soc. 63 (1980) 574–581.
[86] J. Chen, S.J. Bull, Surf. Coat Technol. 201 (2006) 4289–4293.

[87] M. Maxelon, A. Pundt, W. Pyckhout-Hintzen, R. Kirchheim, Scr. Mater. 44 (2001) 817–822.
[88] A. Tehranchi, B. Yin, W.A. Curtin, Philos. Mag. 97 (2017) 400–418.
[89] I.M.A. Ghermaoui, A. Oudriss, A. Metsue, R. Milet, K. Madani, X. Feaugas, Sci. Rep. 9 (2019) 13042.
[90] G. Hachet, A. Oudriss, A. Barnoush, T. Hajilou, D. Wang, A. Metsue, X. Feaugas, Mater. Sci. Eng. A 803 (2020) 140480.
[91] H. Matsui, H. Kimura, A. Kimura, Mater. Sci. Eng. 40 (2) (1979) 227–234.
[92] R. Kirchheim, Scr. Mater. 67 (2012) 767–770.